Materials Advances

ROYAL SOCIETY OF CHEMISTRY

PAPER

View Article Online
View Journal | View Issue

Open Access Article. Published on 03 May 2022. Downloaded on 4/8/2025 2:31:31 AM.
This article is licensed under a Creative Commons Attribution-NonCommercial 3.0 Unported Licence.

Check for updates

Cite this: *Mater. Adv.*, 2022, 3, 4878

In situ topochemically converted 2D $BaTiO_3$ polycrystals with multifarious zone axes†

Fang Kang,‡[ab] Bin Yao,‡[c] Wenxiong Zhang,[d] Fangyi Yao,[e] Qing Zhao,[a] Lei Miao,[a] Fan Zhao,[af] Zhuonan Huang,*[a] Weixing Zhao,[ae] Galhenage Asha Sewvandi,[g] Yifei Wang,*[h] Lixue Zhang,[b] Qi Feng[e] and Dengwei Hu*[a]

$BaTiO_3$ polycrystals with platelike morphology are prepared on the basis of an *in situ* topochemical conversion mechanism from a layered titanate $H_{4x/3}Ti_{2-x/3}\square_{x/3}O_4{\cdot}nH_2O$ (HTO) single crystal as the precursor and different barium compounds. $BaTiO_3$ polycrystals present single-crystal-like electron diffraction points, indicating mesocrystals. The different $BaTiO_3$ mesocrystals present non-uniform zone axes; however, the [100] zone axis of 60% is dominant owing to the intermediate mesocrystalline TiO_2 polymorphs derived from the HTO precursors with the allied TiO_6 octahedral layers. First-principles density functional theory calculations were performed for the verification of the most easily generated $BaTiO_3$(100) surface compared to the other surfaces. $BaTiO_3$ mesocrystals with high purity and multifarious zone axes can be formed using the HTO crystals as a precursor. Furthermore, [100]-textured $BaTiO_3$ ceramics with high density, enhanced degree of orientation, and high piezoelectric constant are fabricated *via* templated grain growth, using the $BaTiO_3$ mesocrystals as templates. Textured $BaTiO_3$ ceramics with excellent physical properties are developed mainly by the growth of oriented template $BaTiO_3$ mesocrystals with the [100] zone axis at the expense of matrix grains, which are $BaTiO_3$ mesocrystals with the non-[100] zone axis. This novel strategy can control the desired orientation of textured materials with high piezoelectric properties.

Received 12th March 2022,
Accepted 30th April 2022

DOI: 10.1039/d2ma00283c

rsc.li/materials-advances

1. Introduction

Owing to its excellent piezoelectric, ferroelectric, and dielectric properties, barium titanate ($BaTiO_3$, BT) with perovskite structure has been widely studied and used in nonvolatile memory devices, actuators, multilayer capacitors, and electro-optic devices.[1–3] Thus far, considerable efforts have been devoted towards the preparation of BT particles, including the hydrothermal method,[4,5] solvothermal method,[6,7] sol–gel method,[8,9] microwave heating method,[10] and solid-state method.[11–13] Among these methods, the solid-state method with its low manufacturing cost, simple but mature technology, and easy removal of additives during the thermal treatment process is conventionally used to synthesize BT materials.[14] The obtained BT particles usually show cubic or spherical morphologies and isotropic character by the normal solid-state reaction. However, piezoelectric materials show crystal-axis anisotropic properties, and high piezoelectricity can be achieved using crystal-axis-oriented materials.[15] Therefore, it is necessary to design a new process to prepare anisotropic crystal-axis-oriented BT particles, such as 1D or 2D BT particles, for the development of piezoelectric materials with excellent properties.

Anisotropic BT particles exhibiting dissimilar facets with intrinsic zone axes have different piezoelectric properties along the directions of the facets. Currently, 2D BT particles mainly present the [110] direction of the zone axis using the hydrothermal method.[7,16,17] However, it is difficult to control the crystal growth and obtain particles with other orientations, such as the [100] direction and [111] direction. Some 2D oriented BT

[a] *Faculty of Chemistry and Chemical Engineering, Engineering Research Center of Advanced Ferroelectric Functional Materials, Key Laboratory of Phytochemistry of Shaanxi Province, Baoji University of Arts and Sciences, 1 Hi-Tech Avenue, Baoji, Shaanxi, 721013, China. E-mail: iceedu@126.com, hdwpolymer@yahoo.co.jp; Fax: +86-(0)917-356-6366; Tel: +86-(0)917-356-6055*
[b] *State Key Laboratory for Mechanical Behavior of Materials, School of Materials Science and Engineering, Xi'an Jiaotong University, Xi'an, 710049, China*
[c] *School of Aerospace Science & Technology, Xidian University, Xi'an, 710071, P. R. China*
[d] *Institute for Solid State Physics, The University of Tokyo, Koto, Sayo, Hyogo 679-5148, Japan*
[e] *Department of Advanced Materials Science, Faculty of Engineering and Design, Kagawa University, 2217-20 Hayashi-cho, Takamatsu-shi, 761-0396, Japan*
[f] *School of Microelectronics, Xi'an Jiaotong University, Xi'an 710049, China*
[g] *Department of Materials Science and Engineering, Faculty of Engineering, University of Moratuwa, Katubedda, Sri Lanka*
[h] *Electrical Insulation Research Center, Institute of Materials Science, University of Connecticut, 97 N Eagleville Rd, Storrs, CT 06269, USA. E-mail: y.wang@uconn.edu*

† Electronic supplementary information (ESI) available: Fig. S1–S11 and Tables S1–S5. See DOI: https://doi.org/10.1039/d2ma00283c

‡ These authors contributed equally to this work.

© 2022 The Author(s). Published by the Royal Society of Chemistry

Open Access Article. Published on 03 May 2022. Downloaded on 4/8/2025 2:31:31 AM. This article is licensed under a Creative Commons Attribution-NonCommercial 3.0 Unported Licence.

particles with different zone axes have been prepared by other methods. A ferroelectric BT thin film with the [110] direction has been prepared by metal–organic chemical vapor deposition (MOCVD) at atmospheric pressure on *p*-type [110] Si wafers as a template.[18] Previously, we showed that platelike BT crystals can be prepared using a hydrothermal soft chemical process with the zone axis in the [110] direction.[16] Further, [001]-poled orthorhombic BT crystals with a high piezoelectric constant can be prepared.[19] BT single crystals can be grown by a top-seeded solution growth (TSSG) method, and they show a crystal-axis orientation along the $[111]_c$ direction; d_{33} along the $[111]_c$ direction of BT single crystals can reach 224 pC N^{-1}.[20] A highly [110]-oriented BT nanorod array can be prepared using a three-step hydrothermal reaction on glass substrates,[17] and the architecture of such a nanorod array is the same as that of mesocrystals. Although considerable improvements have been achieved, intentional control of the direction of the zone axis of 2D BT particles is still extremely difficult because the crystal structure conversion should be self-adjusted to satisfy the principle of minimum energy and space requirements.[21]

The development of BT mesocrystals may be another interesting way to control the direction of the zone axis and improve the piezoelectric properties. Mesocrystals, which are polycrystals with a crystalline array consisting of well-aligned oriented nanocrystals, have attracted considerable attention.[22–24] Various perovskite titanate mesocrystals have been reported.[25] Sphere-like and confetti-like mesocrystals of BT particles have been prepared under ultrasonic irradiation.[26] $SrTiO_3$ mesocrystals have been successfully formed by hydrothermal crystallization using single-crystal anatase nanowires as the precursor.[27] A mesostructured $SrTiO_3/BaTiO_3$ composite film with highly stable ferroelectric properties was developed using a surfactant-templated sol–gel method.[28] We have also developed some titanate mesocrystals using a layered $H_{4x/3}Ti_{2-x/3}\square_{x/3}O_4{\cdot}nH_2O$ (x = 0.8, abbreviated as HTO, □: vacancy of Ti) single crystal as the precursor in our previous studies.[29–31] A mesocrystalline $BaTiO_3/SrTiO_3$ nanocomposite with the [110] zone axis,[29] $Bi_{0.5}Na_{0.5}TiO_3$ (BNT) mesocrystal with the [100] zone axis,[30] and $KNbO_3$ mesocrystal with the [100] zone axis[32] exhibit higher piezoelectric properties than their corresponding isotropic materials.

However, to the best of our knowledge, control of the direction of the zone axis of platelike 2D BT particles prepared by the solid-state process using HTO single crystals as the precursor has not been reported thus far, and few studies have reported the preparation of textured BT ceramics using the TGG process with 2D BT mesocrystals as a template. In the present study, based on a topochemical mesocrystal conversion mechanism, we have designed an interesting route to control the direction of the zone axis of platelike BT particles derived from HTO single crystals and five different barium compounds. The obtained platelike BT particles are polycrystals consisting of BT nanocrystals. Interestingly, they present single-crystal-like electron diffraction points, implying that they are mesocrystals. Moreover, the selective area electron diffraction of the BT mesocrystals confirms that the [100] direction is more dominant than the [110] direction, [111] direction, and so on. Furthermore, textured BT ceramics with high [100] direction orientation, high relative density and good piezoelectric property were fabricated using the BT mesocrystals with the [100] direction as a template and BT mesocrystals with other directions as matrix particles *via* the TGG process. In summary, the fabrication strategy of textured materials can be adopted for the development of high-performance piezoelectric materials.

2. Experimental procedure

2.1 Preparation of the BT particle specimens

All the reagents in this study were of analytical grade and used without further purification. A layered HTO single crystal was prepared *via* the acid treatment of the platelike $K_{0.8}Ti_{1.73}Li_{0.27}O_4$ (KTLO) crystal reported in our previous study. $Ba(OH)_2{\cdot}8H_2O$, $Ba(Ac)_2$, $Ba(NO_3)_2$, $BaCO_3$, and $Ba[CH_3(CH_2)_{16}COO]_2$ were selected as Ba sources in the reactive processes to carry out the crystal structure conversion of the BT particles. A mixture of platelike HTO (0.096 g) and $Ba(OH)_2{\cdot}8H_2O$ (molar ratio of Ba/Ti = 1.25) was ball-milled using a planetary ball mill (PlanetM2-3, Gokin Planetaring, Japan) at a rotational speed of 300 rpm for 24 h. Zirconia balls (3/4 mass content) with a diameter of 5 mm and 5 mL alcohol solution were added to the mill pot. After ball milling and drying at 50 °C, the mixture specimens were calcined in air at 400–900 °C for the desired time. After naturally cooling to room temperature, the specimens were washed with 0.5 mol·L^{-1} acetic acid solution, distilled water, and alcohol in sequence. Finally, the obtained specimens were dried at 50 °C for 12 h. For comparison of the zone axis for the obtained 2D crystals, other compounds of Ba, such as $Ba(NO_3)_2$, $Ba(Ac)_2$, $BaCO_3$, and $Ba[CH_3(CH_2)_{16}COO]_2$ instead of $Ba(OH)_2{\cdot}8H_2O$, were used to carry out the reaction according to the process described above.

2.2 Fabrication of the textured BT ceramic specimens

The textured BT ceramic specimens were fabricated using the TGG process. The starting materials of the prepared BT mesocrystals and BT matrix powder were mixed thoroughly according to a series of Ti mole ratios, *i.e.*, 0 : 10, 0.5 : 9.5, 1 : 9, 1.5 : 8.5, 2 : 8, and 3 : 7. These well-mixed starting material mixtures (0.57 g) with a solvent (3 g 60 vol% toluene–40 vol% ethanol), binder (0.08 g polyvinyl butyral (PVB)), and plasticizer (74 mL di-*n*-butyl phthalate (DBP)) were milled by ball milling with zirconia balls having a diameter of 5 mm at a rotational speed of 60 rpm for 48 h. The resultant slurry was cast on a polyethylene terephthalate (PET) film tape to form a green sheet using an auto film applicator (Tester Sangyo, PI-1210 Filmcoater) by the doctor blade technique. After drying at room temperature, the green sheet was stacked into 128 layers with a size of 13 mm × 13 mm and then pressed at 2 MPa for 3 min at room temperature to form a green compact with a thickness of around 3 mm. Then, the green compacts were heated at a heating rate of 2 °C min^{-1} in three stages at 500 (first stage), 900 (second stage), and 1200–1300 °C (third stage) for 3 h each.

Open Access Article. Published on 03 May 2022. Downloaded on 4/8/2025 2:31:31 AM. This article is licensed under a Creative Commons Attribution-NonCommercial 3.0 Unported Licence.

Finally, the sintered specimens naturally cooled down to room temperature.

2.3 Physical characterization

The structures of the crystalline BT particles and ceramic specimens were investigated using powder X-ray diffraction (XRD) (Shimadzu, XRD-6100) with Cu Kα (λ = 0.15418 nm) radiation. The sizes and morphologies of the specimens were characterized using scanning electron microscopy (SEM) (JEOL, JSM- 5500 S). The nanostructures and zone axes of the mesocrystalline specimens were investigated in detail using transmission electron microscopy (TEM) and selected area electron diffraction (SAED) (JEOL, JEM-3010) at 300 kV, in which the specimens were supported on a Cu microgrid. The zone axes of the 2D BT particle specimens were calculated from the SAED data. The 3D structures and surface morphologies of the specimens were observed by scanning probe microscopy (SPM) (Bruke, Dimension Icon). A spectrometer (Renishaw, Renishaw in Via) was used to measure the Raman spectra of the BT mesocrystals. The degree of orientation (Lotgering factor, F) of the ceramic specimens in the [100] direction was evaluated from the diffraction peak density of XRD in the range of 3°–60° using Lotgering's formula:[33]

$$F = \frac{P - P_0}{1 - P_0}, \quad P = \frac{\sum I(h00)}{\sum I(hkl)}, \quad P_0 = \frac{\sum I_0(h00)}{\sum I_0(hkl)}$$

where I and I_0 are the intensities of the (hkl) peaks for the textured and non-textured specimens, respectively. The F value ranges from 0 to 1, where F = 0 and 1 correspond to completely random and perfectly oriented. The BT ceramic specimen prepared using anatase and $BaCO_3$ as starting materials *via* the conventional solid-state reaction was used as the non-textured standard for evaluating the P_0 value.

For the measurement of the piezoelectric characteristics using a 31 resonator, the BT ceramic specimens were cut into 2.0 mm × 2.0 mm × 0.5 mm (0.5 mm//[100]) pieces with a crystal cutter and polished with diamond slurry. Gold electrodes were fabricated on the top and bottom surfaces with an area of 2.0 mm × 2.0 mm by sputtering. The piezoelectric constant d_{33} was measured at room temperature using a quasi-static d_{33} tester.[34]

2.4 Density functional theory (DFT) calculation details

First-principles density functional theory calculations were performed using the Perdew–Burke–Ernzerhof generalized gradient approximation (GGA-PBE) and the projector augmented wave (PAW) method,[35–37] as implemented in the Vienna Ab-initio Simulation Package (VASP)[38]. Calculations for bulk $BaTiO_3$ (tetragonal, P4mm) were performed with an 8 × 8 × 8 Monkhorst–Pack (MP) special mesh in k-space. For the geometry optimization of the $BaTiO_3$(001), (010), (101), (−110), (011) and (111) (1 × 1) slabs, a Γ-centred MP grid with a 0.03 Å^{-1} separation was used, corresponding to the 8 × 8 × 1, 8 × 8 × 1, 6 × 8 × 1, 8 × 6 × 1, 8 × 6 × 1 and 7 × 7 × 1 meshes in k-space. The plane-wave basis set cutoff was set to 500 eV in all calculations. The convergence threshold was set to smaller than 10^{-6} eV in energy and 0.02 eV·Å^{-1} in force.

However, standard DFT usually causes artificial electron delocalization and fails to describe appropriately the strong correlation between the d electrons in $BaTiO_3$. Therefore, an intra-site Coulomb repulsion U-term was incorporated in the calculations; this was called GGA+U method.[39] A U value of 2.6 eV was used, whose efficacy has been proven for the Ti 3d electrons of the $BaTiO_3$ crystal.[40] The pseudopotentials utilized the valence state of $5s^25p^66s^2$ for Ba, $3s^23p^63d^24s^2$ for Ti, and $2s^22p^4$ for O.

3. Results and discussion

3.1 The phase and microstructure transformation in reaction systems

In this study, we attempt to control or/and change the zone axis of the platelike BT particles prepared using HTO as a precursor and five different barium compounds as barium sources by the solid-state reaction. The barium compounds include $Ba(OH)_2{\cdot}8H_2O$, $Ba(Ac)_2$, $Ba(NO_3)_2$, $BaCO_3$, and $Ba[CH_3(CH_2)_{16}COO]_2$. The BT particles were first prepared by the solid-state reaction using HTO and $Ba(OH)_2{\cdot}8H_2O$ as starting materials, which were calcined at the desired temperatures for 3 h. The XRD patterns of the specimens are shown in Fig. 1A. At 400–500 °C, a few weak characteristic diffraction peaks of the BT phase (JCPDS. No. 31-0174) with perovskite structure are observed, which indicate the occurrence of the BT phase (Fig. 1A-a and b). However, beyond this range, traces of the anatase TiO_2 phase (JCPDS. No. 21-1272) with the characteristic (101) peak are generated (Fig. 1A-a and b), suggesting that the unreacted HTO is transformed into anatase TiO_2. In particular, a mixture of the BT and anatase TiO_2 phases is produced when the calcination temperature of the mixed specimen is elevated to 600 °C (Fig. 1A-c), and the BT phase showed very strong diffraction peaks. As the temperature increases to 800 °C, the diffraction peak intensity of the BT phase decreases while that of the anatase TiO_2 increases obviously (Fig. 1A-d). When the sintering temperature reaches 900 °C, the strong BT phase is observed and the anatase TiO_2 phase disappears, while traces of the rutile TiO_2 phase (JCPDS. No. 21-1276) are generated (Fig. 1A-d).

Microstructure observations and SAED investigations were performed to further clarify the compositions of the reacted products. The TEM images of the specimens show a platelike morphology after calcination at 600 °C (Fig. 1B-a–c), which is in agreement with the SEM image results (Fig. S1, ESI†). It is found that the platelike specimens consist of nanocrystals, indicating that they are polycrystals. Interestingly, their SAED patterns show single-crystal-like diffraction spots (Fig. 1B-b and d). One set of diffraction spots can be assigned to the (001) and (011) planes of the BT phase located along the [100] zone axis (Fig. 1B-b). The other set of diffraction spots can be assigned to the (−111) and (−110) planes of the BT phase located along the [110] zone axis and the (200) and (024) planes of the anatase phase located along the [0−21] zone axis, as shown in Fig. 1B-d.

© 2022 The Author(s). Published by the Royal Society of Chemistry

Open Access Article. Published on 03 May 2022. Downloaded on 4/8/2025 2:31:31 AM.
This article is licensed under a Creative Commons Attribution-NonCommercial 3.0 Unported Licence.

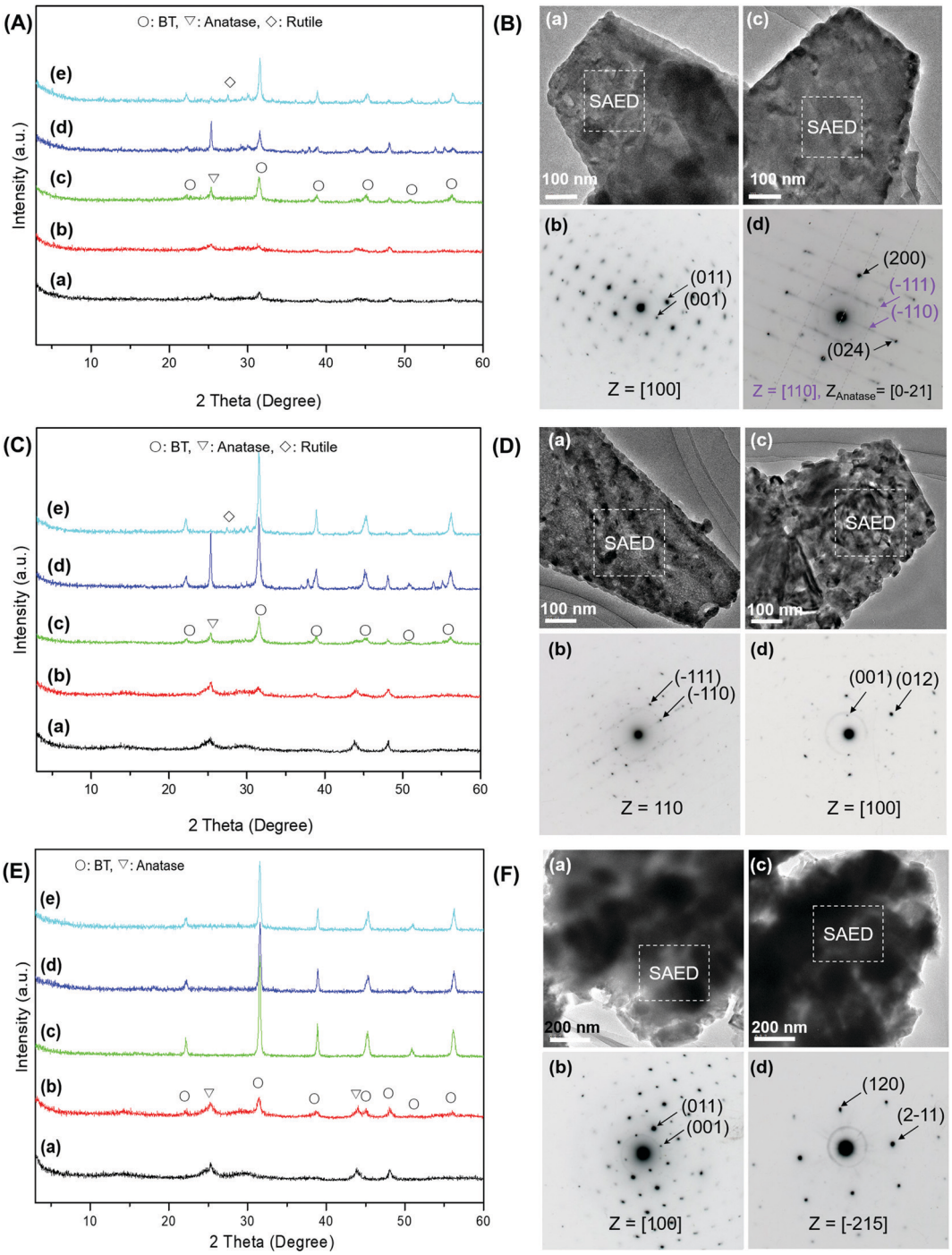

Fig. 1 (A) XRD patterns of the specimens obtained by the calcination of HTO and $Ba(OH)_2{\cdot}8H_2O$ mixed powders at (a) 400, (b) 500, (c) 600, (d) 800, and (e) 900 °C for 3 h. (B) (a, c) TEM images and (b, d) SAED patterns of the specimens obtained by the calcination of HTO and $Ba(OH)_2{\cdot}8H_2O$ mixed powders at 600 °C for 3 h. (C) XRD patterns of the specimens obtained by the calcination of HTO and $Ba(Ac)_2$ mixed powders at (a) 400, (b) 500, (c) 600, (d) 800, and (e) 900 °C for 3 h. (D) (a, c) TEM images and (b, d) SAED patterns of the specimens obtained by the calcination of HTO and $Ba(Ac)_2$ mixed powders at 600 °C for 3 h. (E) XRD patterns of the specimens obtained by the calcination of HTO and $Ba(NO_3)_2$ mixed powders at (a) 400, (b) 500, (c) 600, (d) 800, and (e) 900 °C for 3 h. (F) (a and c) TEM images and (b and d) SAED patterns of the specimens obtained by the calcination of HTO and $Ba(NO_3)_2$ mixed powders at 600 °C for 3 h.

These results imply that the obtained platelike particles are BT/anatase nanocomposite mesocrystals. Different platelike BT mesocrystals exhibit non-uniform zone axes, *i.e.*, different crystal-axis orientations. To determine the dominant zone axis of the platelike BT mesocrystals, 24 random BT mesocrystals were selected for investigation. The results, listed in Table S1 (ESI†), show that six different types of zone axes can be identified, and the [100] and [110] directions are dominant.

Open Access Article. Published on 03 May 2022. Downloaded on 4/8/2025 2:31:31 AM. This article is licensed under a Creative Commons Attribution-NonCommercial 3.0 Unported Licence.

The [100] direction has the highest occurrence probability (54.2%). These results further indicate that the platelike BT mesocrystals exhibit non-uniform zone axes. It is not yet known whether other barium compounds, such as $Ba(OH)_2$, can react with HTO to form BT mesocrystals, and it will be interesting to see whether the formed BT mesocrystals exhibit non-uniform zone axes as well.

We next studied the HTO and $Ba(Ac)_2$ reaction system. As shown in Fig. 1C-a, the BT phase was not formed at 400 °C, suggesting that $Ba(Ac)_2$ is less reactive than $Ba(OH)_2$. The weak diffraction peaks of (110) of BT and (101) of anatase TiO_2 emerged at 500 °C (Fig. 1C-b). As the temperature increased, the intensity of the diffraction peaks of both BT and anatase TiO_2 increased continuously (Fig. 1C-a–d), indicating that the amount and crystallinity of the two specimens increased. After sintering above 900 °C, the strong diffraction peaks of BT and anatase TiO_2 disappeared, and an extremely weak diffraction peak of rutile TiO_2 appeared (Fig. 1C-e). In addition, it is found that the obtained specimens show platelike morphology (Fig. S2 (ESI†) and Fig. 1D), and only one type of single-crystal-like perovskite SAED spot pattern is observed in one platelike particle. The crystal facets of (−111) and (−110) located along the [110] zone axis and (001) and (012) located along the [100] zone axis of BT were obtained (Fig. S2, ESI†). The results of the investigation of 14 random BT mesocrystals are listed in Table S2 (ESI†). As seen from the table, the [100] direction has the highest occurrence probability, which is around 42.9%, followed by the [110] direction, similar to the HTO and $Ba(OH)_2$ reaction system.

As the BT phase obtained in the HTO-$Ba(OH)_2{\cdot}8H_2O$ and HTO-$Ba(Ac)_2$ reaction systems is impure, we next studied the reaction system using $Ba(NO_3)_2$, $BaCO_3$ and $Ba[CH_3(CH_2)_{16}COO]_2$ as barium sources. As shown in Fig. 1E-a, for the HTO-$Ba(NO_3)_2$, system, after calcination at 400 °C, the main diffraction peaks of the product were the anatase TiO_2 phases, and the characteristic peaks of BT were also clearly observed. The specimen contained a small amount of the anatase TiO_2 phase and a large amount of BT at 500 °C (Fig. 1E-b). It is worth noting that as the calcination temperature increases over 600 °C, the TiO_2 phase disappears, thereby achieving the pure BT phase (Fig. 1E-c). To further clarify the phase composition and zone axis of the specimen obtained by the calcination of the mixed powders of HTO and $Ba(NO_3)_2$ at 600 °C for 3 h, the SEM and TEM images and SAED patterns were studied. It is found that the specimens show a platelike morphology (Fig. S3 (ESI†) and Fig. 1F). The SAED pattern shows the 011 and 001 single-crystal-like diffraction spots of BT located along the [100] zone axis (Fig. 1F). Furthermore, 120 and 2−11 diffraction spots of BT are observed in Fig. 1F-d, suggesting that the [−215] direction for the BT nanocrystals is still achieved. These results indicate that different platelike BT mesocrystals with different facets can be prepared using the HTO-$Ba(NO_3)_2$ reaction system. The occurrence probabilities of the zone axes of the platelike BT mesocrystals are listed in Table S3 (ESI†). The [100] and [110] directions are dominant and the [100] direction has the highest occurrence probability of up to 60%. These results imply that the BT mesocrystal prepared using $Ba(OH)_2$ or $Ba(Ac)_2$ as a raw material is a mixture of BT and TiO_2 phases, while that prepared by sintering HTO and $Ba(NO_3)_2$ mixed powder is a pure BT phase. The occurrence probabilities of the zone axes for the BT mesocrystals are nearly the same when different barium compounds are used as the starting materials.

The pure BT phase was also obtained in the HTO-$BaCO_3$ and HTO-$Ba[CH_3(CH_2)_{16}COO]_2$ reaction systems, as indicated in Fig. S4 and S5 (ESI†). The nanostructures and zone axes of the specimen obtained by the calcination of HTO-$BaCO_3$ mixed powders at 800 °C for 3 h were investigated using TEM and SEAD, as shown in Fig. S4B (ESI†). It is easy to observe a set of single-crystal-like SAED spots for the BT phase with the [11-4] and [100] zone axes located on the basal plane (Fig. S4B-b and d, ESI†), which also indicates that the BT mesocrystal with platelike morphology (Fig. S4B-a and c and S6, ESI†) can be generated under 800 °C for 3 h. The obtained BT mesocrystals also show different zone axes. It can also be confirmed that the platelike BT particles produced from the HTO-$Ba[CH_3(CH_2)_{16}COO]_2$ reaction system are also constructed from nanoparticles (Fig. S5B-a and c and S7, ESI†). In the corresponding SAED patterns (Fig. S5B-b and d, ESI†), a set of SAED spots can be assigned to the (001) and (110) planes of the BT mesocrystal located along the [110] zone axis. Single-crystal diffraction spots assigned to the (001) and (012) planes of the BT mesocrystal are also observed, indicating that the obtained BT mesocrystal also shows different zone axes. The occurrence probability of the zone axes for the BT mesocrystals is calculated as shown in Table S4 (ESI†). The [100], [110], and [1−1−4] directions are dominant, and the occurrence probability of the [100] direction is relatively high.

To determine the impact of the raw materials on the zone axes of the specimens, we selected the most reactive $Ba(NO_3)_2$ and the least reactive $Ba(Ac)_2$ for further investigation. The XRD patterns of the products obtained by the prolonged calcination of the HTO-$Ba(Ac)_2$ and HTO-$Ba(NO_3)_2$ mixed powders at 500 °C are shown in Fig. S8 (ESI†). The peak intensity of anatase TiO_2 obtained from the HTO-$Ba(NO_3)_2$ reaction system is much lower than that obtained from the HTO-$Ba(Ac)_2$ reaction system (Fig. S8a and b, ESI†), which indicates that the obtained product has higher purity at 500 °C for 15 h than for 3 h and further implies that $Ba(NO_3)_2$ has high reactivity. The pure BT phase with strong diffraction peaks can be obtained from the HTO-$Ba(NO_3)_2$ reaction system when the reaction time is extended to 18 h (Fig. S8, ESI†), suggesting that BT has high crystallinity. The corresponding SEM images of the specimens with platelike morphology are also shown in Fig. 2A. This result indicates that platelike BT particles with a mean size of 1.31 μm (Fig. 2A-d) can be obtained by the calcination of HTO and $Ba(NO_3)_2$ mixed powders at 500 °C for 18 h, and it can be used as a suitable template for the fabrication of textured BT ceramics.

Fig. 2B shows the TEM images and SAED patterns of the specimens obtained by the calcination of HTO and $Ba(NO_3)_2$ mixed powders at 500 °C for 18 h. The platelike polycrystalline specimens are constructed from nanoparticles with a size of around 50 nm (Fig. 2B-a and c). Different orientations are observed from dissimilar platelike BT mesocrystals, which

 © 2022 The Author(s). Published by the Royal Society of Chemistry

Open Access Article. Published on 03 May 2022. Downloaded on 4/8/2025 2:31:31 AM.
This article is licensed under a Creative Commons Attribution-NonCommercial 3.0 Unported Licence.

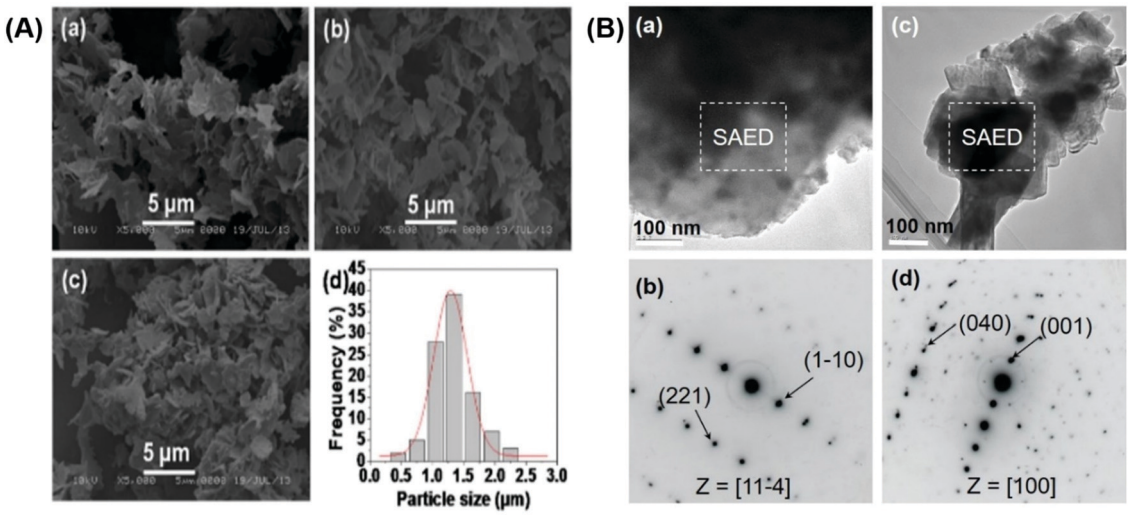

Fig. 2 (A) SEM images of the specimens obtained by the calcination of HTO and (a) $Ba(Ac)_2$ and (b and c) $Ba(NO_3)_2$ mixed powders at 500 °C for (a and b) 15 h and (c) 18 h. (A) (d) shows the particle size distribution of the specimens shown in the SEM image of (A) (c). (B) (a and c) TEM images and (b and d) SAED patterns of the specimens obtained by the calcination of HTO and $Ba(NO_3)_2$ mixed powders at 500 °C for 18 h.

include the orientation of the [110] and [100] zone axes of the nanoparticles (Fig. 2B-b and d). As seen from Table S5 (ESI†), the [100] and [110] directions are the main zone axes, and the occurrence probability of over 60% of the [100] direction is still higher than that of the [110] direction. These results indicate that platelike BT mesocrystals with different facets can be obtained after prolonged calcination of the mixture of HTO and $Ba(NO_3)_2$ powders.

The results suggest that pure platelike BT mesocrystals can be prepared by the prolonged reaction of HTO and $Ba(NO_3)_2$ at 500 °C. All the BT mesocrystals are constructed from the oriented nanocrystal with the same crystal axis. Moreover, among these zone axes of the platelike BT mesocrystals, the [100] direction has the highest occurrence probability, followed by the [110] direction. To the best of our knowledge, this is the first study to demonstrate that different products obtained from the same reaction have different zone axes, in contrast to only the [100] zone axis of the platelike BT particles prepared by a solvothermal process in $Ba(OH)_2{\cdot}8H_2O$ solution.[16,29] Such 2D BT mesocrystals could be regarded as a promising candidate template for fabricating textured ceramics with high piezoelectric properties. The microstructure of 2D BT mesocrystals requires further investigation.

3.2 Investigation of the microstructures of BT polycrystals

The 2D and 3D morphologies of the BT polycrystals and the microstructures of the multi-crystal-oriented BT polycrystals were investigated *via* atomic force microscopy (AFM) and Raman scattering. Fig. S9 (ESI†) shows the AFM images of the 2D and 3D morphologies of the platelike BT mesocrystals obtained by the calcination of mixtures of HTO-$Ba(Ac)_2$ and HTO-$Ba(NO_3)_2$ at 500 °C for 15 and 18 h, respectively. The nanoscale BT particles aligned with each other on the platelike particles are uniformly distributed, while the rough surfaces of the specimens are observed under the bright and dark paths. The nanoparticles of BT are more uniformly distributed in the case of the HTO and $Ba(NO_3)_2$ reaction system at 500 °C for 18 h. These results are consistent with the TEM results (Fig. 2B-a and c). The Raman spectra for anatase TiO_2 and the specimens obtained by different reaction systems are shown in Fig. S10 (ESI†). The anatase TiO_2 phase, which belongs to the tetragonal system, shows Raman scattering bands at around 144, 396, 518, and 639 cm^{-1}, which can be assigned to the E_g, B_{1g}, A_{1g}, and B_{1g} modes, respectively (Fig. S10a, ESI†).[41] Among them, the band at 144 cm^{-1} is the symmetrical-type O–Ti–O variable angle vibration peak with the strongest intensity, which is the characteristic peak of the anatase TiO_2 phase. It is well known that the main Raman scattering bands at around $250A_1$(TO), $306B_1$, 520 [E(TO), A_1(LO)], and 720 [E(TO), A_1(LO)] cm^{-1} correspond to the tetragonal BT phase.[42,43] The Raman spectra of the specimens obtained by different reaction systems at 600 °C for 3 h are the same as the bands of the anatase TiO_2 phase (Fig. S10b–f and d–f, ESI†), which means that the main phase of the specimen is still the TiO_2 phase. However, strong bands for the tetragonal BT phase (Fig. S10b–d, ESI†) in the HTO-$Ba(NO_3)_2$, HTO-$Ba(OH)_2$, and HTO-$Ba(Ac)_2$ reaction systems can be confirmed, while strong bands for the anatase phase (Fig. S12e and f, ESI†) in the HTO-$BaCO_3$ and HTO-$Ba[CH_3(CH_2)_{16}COO]_2$ reaction systems can be observed. This result is consistent with the XRD results (Fig. 1A, 1C, 1E and Fig. S4A, S5A, ESI†) and further illustrates the reactivity sequence of the barium compounds.

It is worth noting that the band at 120–125 cm^{-1} might be derived from the strain between the BT phase and the anatase phase. To show that strain exists in the BT mesocrystal nanostructure, pure platelike BT mesocrystals obtained by the calcination of HTO and $Ba(NO_3)_2$ mixed powders at 500 °C for 18 h were investigated further. The Raman spectra and mapping are shown in Fig. 3. Ten strips of nearly the same Raman spectra (Fig. 3A) are derived from 10 equidistant points selected

Open Access Article. Published on 03 May 2022. Downloaded on 4/8/2025 2:31:31 AM.
This article is licensed under a Creative Commons Attribution-NonCommercial 3.0 Unported Licence.

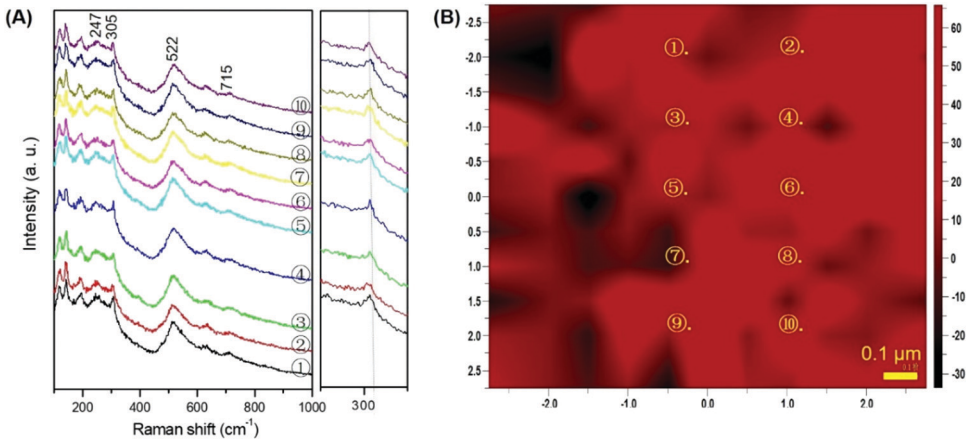

Fig. 3 (A) Raman spectra and (B) Raman mapping of BT mesocrystals obtained by the calcination of HTO and $Ba(NO_3)_2$ mixed powders at 500 °C for 18 h.

in the Raman mapping (Fig. 3B). Each of these spots in Fig. 3B is the Raman signal of the 2D polycrystalline specimen, which corresponds to the Raman spectrum in Fig. 3A. Each spectrum presents the similar typical tetragonal BT phases, suggesting that the constructed nanoparticles of the specimen are uniformly distributed. However, unlike the reported Raman spectra of tetragonal BT,[44,45] the Raman spectra of the tetragonal BT mesocrystals prepared in this study show multiple bands below 200 cm^{-1}, which could be attributed to the in-plane compressive stress induced by the strain derived from the interior of the mesocrystals. This result also implies that the tetragonal BT mesocrystals are constructed from crystal-axis-oriented nanocrystals, giving rise to multiple in-plane bending vibrations of different Ti–O bonds from the BT products. This can also be verified by the bands with a uniform position of around 306 cm^{-1} shown in the magnified view in Fig. 3A. The Raman spectra for anatase TiO_2 and the specimens obtained by different reaction systems indicate that a single BT mesocrystal only has its own stress and no external stress, *i.e.*, the obtained BT mesocrystals without stress are nearly uniform. All the above-mentioned results suggest not only that the distribution of nanocrystals of BT mesocrystals is uniform but also that a single BT mesocrystalline grain has only one type of crystal direction.

3.3 Formation mechanism of the multi-crystal-oriented BT polycrystals

To better understand why the [100] direction has the highest occurrence probability among the zone axes of the platelike BT mesocrystals, the surface energies of the relaxed $BaTiO_3$ (001), (010), (101), (−110), (011) and (111) surfaces were calculated. Before the calculation, the bulk properties of $BaTiO_3$ were first calculated, as shown in Fig. S11 (ESI†).

Fig. 4A shows the optimized structures of the $BaTiO_3$ (001), (010), (101), (−110), (011) and (111) surfaces with different terminated, computations are performed using a (1 × 1) unit cell with 4 atomic layers and a vacuum layer with a thickness of 15 Å. The calculated surface energies of the relaxed $BaTiO_3$(001), (010), (101), (−110), (011) and (111) surfaces are listed in Table 1. The surface energies calculated for $BaTiO_3$ (010) with TiO_2 and BaO-terminated have only a small difference (0.0514 and 0.0605 eV·Å^{-2}, respectively). However, for the $BaTiO_3$ (011) and (101) surfaces, different terminations have great differences in their surface energies, and the O-terminated surface has the smallest energy (0.0895 eV·Å^{-2}). This means that the O-terminated $BaTiO_3$ (011) and (101) surfaces are more stable than the BaTiO-terminated surface. The surface energy calculated for $BaTiO_3$ (111) with BaO-terminated is 0.1078 eV·Å^{-2}. Therefore, the surface energies of $BaTiO_3$ are in increasing order as follows: (010) surface < (001) surface < (011) surface = (101) surface < (−110) surface < (111) surface, which shows that the $BaTiO_3$(010) and (001) facets are relatively easy to expose on the surface. This conclusion is in agreement with our experimental results, since the $BaTiO_3$(010) and (001) surfaces correspond to the [100] zone axis.

In general, the microstructures of the obtained products under the same reaction conditions are the same or similar to each other. However, in this study, the zone axes of the BT mesocrystals obtained from the reactions of the HTO single crystal and the barium compounds are different. This can be ascribed to the precursor HTO and the allied TiO_6 octahedral layers of the reaction process. The mechanism for the formation of BT polycrystals with multiple zone axes from the HTO crystal is proposed, as shown in Fig. 4B. After calcination in the temperature range of 500–600 °C, the HTO crystal can generate different TiO_2 polymorph polycrystals, such as TiO_2 (B), which may be the twinning of TiO_2 $(B)_1$ and TiO_2 $(B)_2$, anatase, and rutile.[21] In this case, during the reaction process of the HTO single crystals and the barium compounds, any type of generated TiO_2 polymorphs derived from the polycrystal may be naturally selected as a seed crystal (left of Fig. 4B), and the other titanium sources act as supplements growing around the seed crystals by heteroepitaxial growth to form the crystalline BT phase until they are all consumed. The different seed crystals obtained from the TiO_2 polymorphs result in different orientations of the crystalline BT phase. Therefore, the zone axis of a single platelike crystal is unique, while the zone axes of different single mesocrystals may be different, which are

© 2022 The Author(s). Published by the Royal Society of Chemistry

Open Access Article. Published on 03 May 2022. Downloaded on 4/8/2025 2:31:31 AM.
This article is licensed under a Creative Commons Attribution-NonCommercial 3.0 Unported Licence.

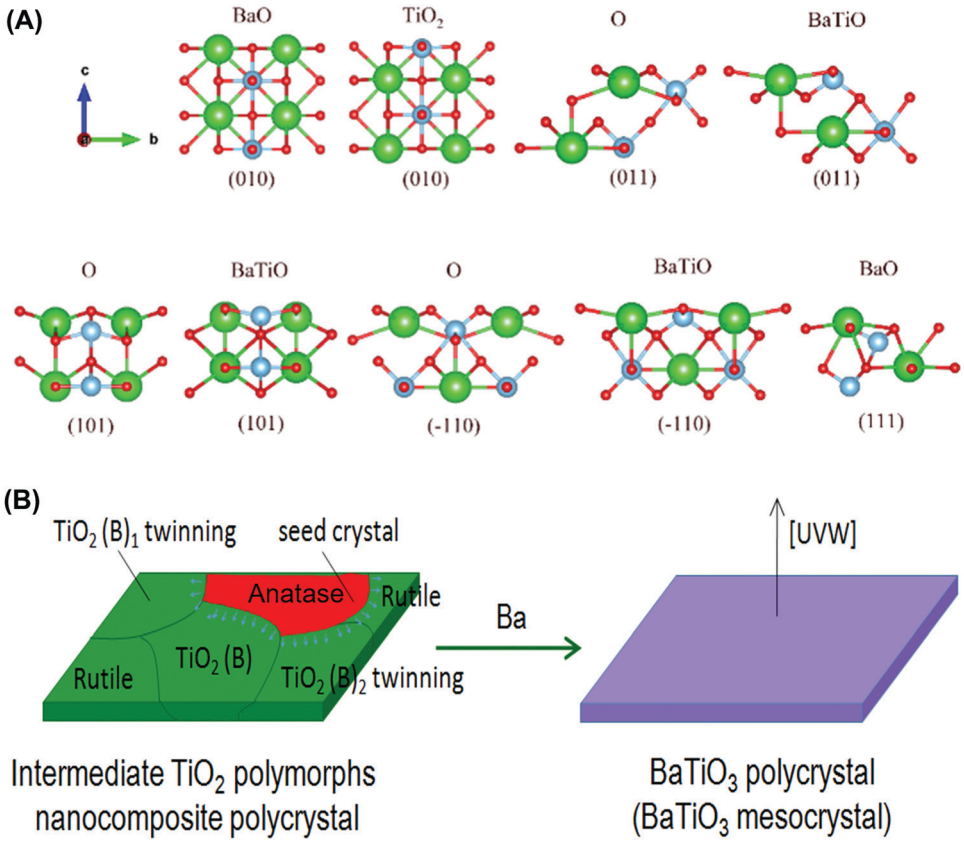

Fig. 4 (A) Optimized structures of the $BaTiO_3$ (010), (011), (101), (−110) and (111) surfaces with different terminations (green, blue and red spheres denote Ba, Ti and O atoms, respectively). (B) Schematic illustration of the proposed mechanism for the formation of BT polycrystals with multiple zone axes from the intermediate TiO_2 polymorph nanocomposite polycrystal derived from the HTO single crystal after thermal treatment.

Table 1 Calculated surface energies of the relaxed $BaTiO_3$ (001), (010), (011), (101), (−110) and (111) surfaces with different terminations

Surface	Type	Surface energy ($eV·Å^{-2}$)
(001)	BaO-Terminated	0.0622
(010)	TiO_2-Terminated	0.0514
	BaO-Terminated	0.0605
(011)	O-Terminated	0.0895
	BaTiO-Terminated	0.1214
(101)	O-Terminated	0.0895
	BaTiO-Terminated	0.1212
(–110)	O-Terminated	0.0944
	BaTiO-Terminated	0.1164
(111)	BaO-Terminated	0.1078

consistent with the above-mentioned SAED results. The BT mesocrystals with the [110] orientation using the [010]-oriented anatase as seed crystals are dominant because the [110] direction corresponds to the [010] direction of anatase in the crystal conversion process,[46] which is in accordance with the above-mentioned results.

3.4 Textured BT piezoelectric ceramics fabricated from BT mesocrystals

Texture engineering for the control of the orientation direction of piezoelectric ceramics is an effective method for enhancing their piezoelectricity. The TGG method is widely adopted for the fabrication of textured ceramics. A template might be selected using the platelike BT mesocrystal obtained by the calcination of HTO-$Ba(NO_3)_2$ mixed powders at 500 °C for 18 h, although the 2D BT mesocrystals have multiple zone axes. We also prepared textured BT ceramics *via* the TGG method using a mixture of platelike BT mesocrystals and spherical BT powder with non-orientation as starting materials. Fig. 5A shows the XRD patterns of BT ceramic specimens after sintering at different temperatures using pure platelike BT mesocrystals as materials. The strongest peak was the peak of (200) of the BT ceramics rather than the peak of (110) of the BT mesocrystals, and BT ceramics with the [200] orientation that is equivalent to the [100] orientation were fabricated. The degree of orientation and the relative density of the textured BT ceramics are listed in Table 2. As the sintering temperature increases, the degree of orientation increases from $F_{(200)}$ = 69% at 1200 °C to $F_{(200)}$ = 81% at 1250 °C, whereas the degree of orientation decreases to 64.15% after the temperature increases above 1300 °C. The results are consistent with the dominant [100] zone axis calculated from the SAED data of the obtained platelike BT mesocrystals. Moreover, the degree of the [100] orientation (81%) of the formed ceramics is higher than the occurrence probability (60%) of the [100] zone axis of the BT mesocrystals, suggesting that the orientation may improve after ceramic growth.

Open Access Article. Published on 03 May 2022. Downloaded on 4/8/2025 2:31:31 AM.
This article is licensed under a Creative Commons Attribution-NonCommercial 3.0 Unported Licence.

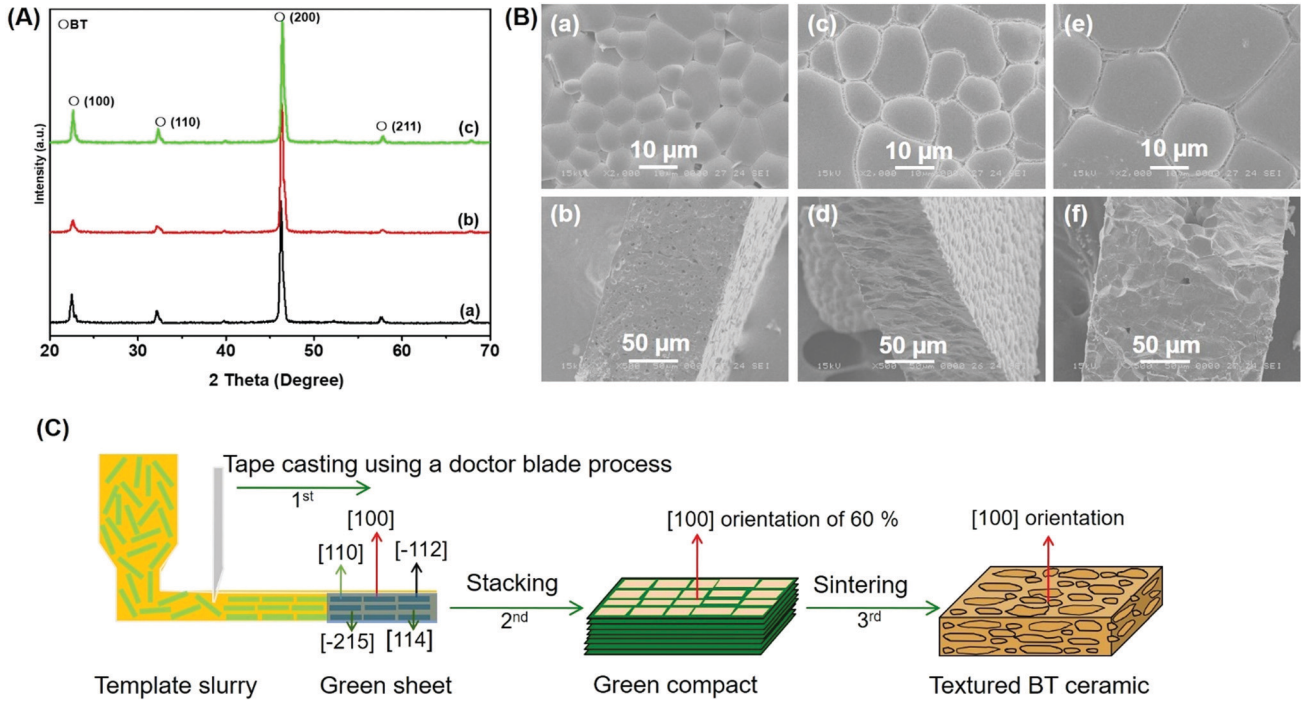

Fig. 5 (A) XRD patterns of the BT ceramic specimens prepared from platelike BT mesocrystals under the different sintering temperatures of (a) 1200, (b) 1250, and (c) 1300 °C. (B) The surfaces (a, c, and e) and (b, d, and f) cross-sectional SEM images of the BT ceramic specimens prepared from the BT mesocrystals at the sintering temperatures of 1200, 1250, and 1300 °C, respectively. (C) Schematic diagram of the formation mechanism of textured BT ceramics with BT mesocrystals as the template.

Table 2 Degree of orientation ([100]) and d_{33} of the textured BT ceramic specimens prepared from BT mesocrystals sintered at different temperatures

No.	Ratio of BT powder/BT mesocrystal	Sintering temperature (°C)	Relative density (%)	Degree of orientation (%)	d_{33} (pC N^{-1})
1	0 : 10	1200	95.27	69	244
2	0 : 10	1250	98.05	81	310
3	0 : 10	1300	96.30	64	295
4[a]	0.5 : 9.5	—		60	—
5	0.5 : 9.5	1250		73	322
6	1 : 9	1250		61	319
7	1.5 : 8.5	1250		43	207

[a] The specimen is the green compact before sintering.

Fig. 5B shows the SEM images of the surfaces and cross sections of the ceramic specimens after sintering at different temperatures. After sintering above 1200 °C, many gaps between the grains and relatively poor density are observed for the BT ceramic specimens in Fig. 5B-a and b. Uniform size, homogeneous microstructure, and high density of the BT ceramics are obtained after sintering at 1250 °C for 3 h (Fig. 5B-c and d). When the sintering temperature further increases to 1300 °C (Fig. 5B-e and f), the density of the prepared specimens decreases. Therefore, the optimum sintering condition of the BT ceramics is 1250 °C for 3 h. We also measured the piezoelectric constant d_{33} of the materials at different temperatures, as shown in Table 2. It is found that the value of d_{33} increases with the treatment temperature, reaching a maximum value at 1250 °C, and then decreases with further increase in temperature.

In addition, as shown in Table 2, the ratio of the BT powder to BT mesocrystal has a significant influence on the degree of orientation and d_{33}. At a ratio of 0.5 : 9.5, after sintering, the degree of the occurrence probability of the [100] zone axis increases from 60% to 73%. At the same time, a high d_{33} value was also obtained. By further increasing the ratio of BT powder to BT mesocrystal, both the degree of orientation and d_{33} decrease. The above-mentioned results indicate that the small grain size, high density, and high degree of orientation of the textured BT ceramic are very promising for high-performance piezoelectric materials.

3.5 Formation mechanism of the textured BT ceramics

The piezoelectric constant (d_{33} = 322 pC N^{-1}) of the textured BT ceramic prepared from the BT powder/BT mesocrystal mixture with a ratio of 0.5 : 9.5 is close to the d_{33} value of the textured BT

© 2022 The Author(s). Published by the Royal Society of Chemistry

Open Access Article. Published on 03 May 2022. Downloaded on 4/8/2025 2:31:31 AM. This article is licensed under a Creative Commons Attribution-NonCommercial 3.0 Unported Licence.

ceramic prepared from the pure BT mesocrystal (310 pC N^{-1}). The formation mechanism of the textured BT ceramic by the TGG method using the platelike BT mesocrystal reaction system is shown in Fig. 5C. In the first step, the template slurry of randomly oriented BT mesocrystals was arranged using a doctor blade to form a green sheet by a tape casting process. The platelike BT mesocrystals with different orientations were aligned to increase the degree of orientation. In the second step, the green sheets with preferred orientation were stacked to form a green compact after densification. In this case, the green compact could be considered as a meaningful composition that is constructed from the oriented templates of 60% and matrix grains of 40%, where the oriented templates are oriented BT mesocrystals with the [100] orientation and the matrix grains are oriented BT mesocrystals with the non-[100] orientation. Therefore, although this is an interesting coincidence, the ratio of the oriented templates and the matrix grains is conducive to the fabrication of high-performance piezoelectric ceramics.[47,48] Finally, the textured BT ceramics can be obtained by three-step calcination. In this process, the oriented BT ceramic is developed mainly by the growth of oriented BT mesocrystal template particles at the expense of matrix grains.[49] The textured BT ceramics exhibit a high piezoelectric property, which is due to the fabricated ceramic with a high degree of orientation, high density, and small grain size. Most importantly, the oriented BT mesocrystal is the raw material with a dominant [100] orientation of 60%, and it is constructed from the nanocrystal with the same crystal axis.

4. Conclusions

The platelike BT mesocrystals can be prepared from platelike HTO single crystals and barium compounds *via* a topochemical mesocrystal conversion mechanism. Further, we showed that BT mesocrystals with high purity and multi-crystal orientation can be prepared using the HTO and $Ba(NO_3)_2$ reaction system at 500 °C. The (100) facet was found to be dominant owing to the allied TiO_6 octahedral layers of the HTO precursors. DFT calculations verify that the $BaTiO_3$(100) surface can be most easily generated compared to the other surfaces. In addition, [100]-textured BT ceramics with high density, a high degree of orientation, and a high piezoelectric constant could be fabricated by the TGG process using BT mesocrystals as raw materials. Textured BT ceramic materials showing a high d_{33} value of 322 pC N^{-1} were realized using the BT powder/BT mesocrystal mixture with a mole ratio of 0.5 : 9.5 as raw materials at a sintering temperature of 1250 °C for 3 h. The textured BT ceramics exhibited a high piezoelectric property owing to the fabricated ceramic with a high degree of orientation, high density, and small grain size. They were developed mainly by the growth of oriented template BT mesocrystals with the [100] zone axis at the expense of matrix grains, which are BT mesocrystals with the non-[100] zone axis. The BT mesocrystal was shown to be suitable for preparing [100]-textured BT ceramics with high density and high piezoelectric properties. In summary, a new target was presented for the development of high-performance piezoelectric materials.

Author contributions

The manuscript was written through contributions of all authors. All authors have given their approval to the final version of the manuscript. Fang Kang: synthesized the sample, analyzed the data, carried out the TEM and SAED characterizations and wrote the manuscript. Bin Yao: analyzed the data and wrote the manuscript. Wenxiong Zhang: performed crystallographic analysis and carried out the TEM and AFM characterizations. Fangyi Yao: performed crystallographic analysis and revised the manuscript. Qing Zhao: synthesized the sample. Lei Miao: synthesized the sample and carried out the Raman spectra and Raman mapping analyses. Fan Zhao: analyzed the data and revised the manuscript. Zhuonan Huang: as one of the corresponding authors, performed the density functional theory calculations. Weixing Zhao: analyzed the TEM and crystal structures. Galhenage Asha Sewvandi: carried out general crystallographic analysis and wrote the manuscript. Yifei Wang: as one of the corresponding authors, analyzed the data and wrote the manuscript. Lixue Zhang: revised the manuscript. Qi Feng: carried out general crystallographic analysis. Dengwei Hu: as a corresponding author, conceived the study and wrote the manuscript with inputs from the other authors.

Conflicts of interest

There are no conflicts to declare.

Acknowledgements

This work was supported in part by the National Natural Science Foundation of China (No. 21005003), the Basic Research Project in Natural Science Foundation of Shaanxi Provincial of China (2019JM-091), the Serving the Local Scientific Research Project in Foundation of Shaanxi Education Department (19JC002), and the Doctoral Scientific Research Starting Foundation of Baoji University of Arts and Sciences (No. ZK2018059).

References

1 B. Dai, P. Zheng, W. Bai, F. L. Li, W. Wu, Z. Ying and L. Zheng, Direct and converse piezoelectric grain-size effects in $BaTiO_3$ ceramics with different Ba/Ti ratios, *J. Eur. Ceram. Soc.*, 2018, **38**, 4212–4219.
2 Y. Huan, X. Wang, J. Fang and L. Li, Grain size effect on piezoelectric and ferroelectric properties of $BaTiO_3$ ceramics, *J. Eur. Ceram. Soc.*, 2014, **34**, 1445–1448.
3 X. Tian, J. Li, K. Chen, J. Han, S. Pan, Y. Wang, X. Fan, F. Li and Z. Zhou, Nearly monodisperse ferroelectric $BaTiO_3$ hollow nanoparticles: Size-related solid evacuation in ostwald-ripening-induced hollowing process, *Cryst. Growth Des.*, 2010, **10**, 3990–3995.

Open Access Article. Published on 03 May 2022. Downloaded on 4/8/2025 2:31:31 AM. This article is licensed under a Creative Commons Attribution-NonCommercial 3.0 Unported Licence.

4 Q. Feng, M. Hirasawa, K. Kajiyoshi and K. Yanagisawa, Hydrothermal soft chemical synthesis and particle morphology control of $BaTiO_3$ in surfactant solutions, *J. Am. Ceram. Soc.*, 2005, **88**, 1415–1420.
5 H. Xu and L. Gao, Hydrothermal synthesis of high-purity $BaTiO_3$ powders: Control of powder phase and size, sintering density, and dielectric properties, *Mater. Lett.*, 2004, **58**, 1582–1586.
6 D. Chen and X. Jiao, Solvothermal synthesis and characterization of barium titanate powders, *J. Am. Ceram. Soc.*, 2000, **83**, 2637–2639.
7 Q. Feng, Y. Ishikawa, Y. Makita and Y. Yamamoto, Solvothermal soft chemical synthesis and characterization of platelike particles constructed from oriented $BaTiO_3$ nanocrystals, *J. Ceram. Soc. Jpn.*, 2010, **118**, 141–146.
8 S. Bisen, A. Mishra and K. M. Jarabana, Studies of ferroelectric and dielectric properties of pure and doped barium titanate prepared by sol–gel method, *AIP. Conf. Proc. AIP. Pub.*, 2016, **1731**, 0500701.
9 W. Wang, L. Cao, W. Liu, G. Su and W. Zhang, Low-temperature synthesis of $BaTiO_3$ powders by the sol–gel-hydrothermal method, *Ceram. Int.*, 2013, **39**, 7127–7134.
10 H. Takahashi, Y. Numamoto, J. Tani and S. Tsurekawa, Piezoelectric properties of $BaTiO_3$ ceramics with high performance fabricated by microwave sintering, *Jpn. J. Appl. Phys.*, 2006, **45**, 7405.
11 K. Jarabana, A. Mishra and S. Bisen, Structural and optical properties of poly-crystalline $BaTiO_3$ and $SrTiO_3$ prepared *via* solid state route, *J. Phys: Conf. Ser., IOP Pub.*, 2016, **755**, 0120201.
12 S. Shao, J. Zhang, Z. Zhang, P. Zheng, M. Zhao, J. Li and C. Wang, High piezoelectric properties and domain configuration in $BaTiO_3$ ceramics obtained through the solid-state reaction route, *J. Phys. D: Appl. Phys.*, 2008, **41**, 125408.
13 M. Buscaglia, M. Bassoli, V. Buscaglia and R. Vormberg, Solid-state synthesis of nanocrystalline $BaTiO_3$: Reaction kinetics and powder properties, *J. Am. Ceram. Soc.*, 2008, **91**, 2862–2869.
14 C. Chungtai, *US Pat.*, US5125070A, 1992.
15 X. Kong, Y. Ishikawa, K. Shinagawa and Q. Feng, Preparation of crystal-axis-oriented barium calcium titanate platelike particles and its application to oriented ceramic, *J. Am. Ceram. Soc.*, 2011, **94**, 3716–3721.
16 Q. Feng, M. Hirasawa and K. Yanagisawa, Synthesis of crystal-axis-oriented $BaTiO_3$ and anatase platelike particles by a hydrothermal soft chemical process, *Chem. Mater.*, 2001, **13**, 290–296.
17 L. Yao, Z. Pan, J. Zhai and H. Chen, Novel design of highly [110]-oriented barium titanate nanorod array and its application in nanocomposite capacitors, *Nanoscale.*, 2017, **9**, 4255–4264.
18 I. Kim, C. Lee and S. Park, Preparation of $BaTiO_3$ thin film by metalorganic chemical vapor deposition using ultrasonic spraying, *Jpn. J. Appl. Phys.*, 1994, **33**, 5125.
19 S. Park, S. Wada, L. Cross and T. Shrout, Crystallographically engineered $BaTiO_3$ single crystals for high-performance piezoelectrics, *J. Appl. Phys.*, 1999, **86**, 2746–2750.
20 K. Yako, H. Kakemoto, T. Tsurumi and S. Wada, Domain size dependence of d_{33} piezoelectric properties for barium titanate single crystals with engineered domain configurations, *Mater. Sci. Eng., B.*, 2005, **120**, 181–185.
21 D. Hu, W. Zhang, Y. Tanaka, N. Kusunose, Y. Peng and Q. Feng, Mesocrystalline nanocomposites of TiO_2 polymorphs: Topochemical mesocrystal conversion, characterization, and photocatalytic response, *Cryst. Growth Des.*, 2015, **15**, 1214–1225.
22 M. Niederberger and H. Cölfen, Oriented attachment and mesocrystals: Non-classical crystallization mechanisms based on nanoparticle assembly, *Phys. Chem. Chem. Phys.*, 2006, **8**, 3271–3287.
23 R. Song and H. Cölfen, Mesocrystals-ordered nanoparticle superstructures, *Adv. Mater.*, 2010, **22**, 1301–1330.
24 X. Yang, J. Qin, Y. Li, R. Zhang and H. Tang, Graphene-spindle shaped TiO_2 mesocrystal composites: Facile synthesis and enhanced visible light photocatalytic performance, *J. Hazard. Mater.*, 2013, **261**, 342–350.
25 N. Park, Y. Wang, W. Seo, F. Dang, C. Wan and K. Koumoto, Solution synthesis and growth mechanism of $SrTiO_3$ mesocrystals, *Cryst. Eng. Comm.*, 2013, **15**, 679–685.
26 F. Dang, K. Kato, H. Imai, S. Wada, H. Haneda and M. Kuwabara, Oriented aggregation of $BaTiO_3$ nanocrystals and large particles in the ultrasonic-assistant synthesis, *CrystEngComm*, 2010, **12**, 3441–3444.
27 V. Kalyani, B. Vasile, A. Ianculescu, M. Buscaglia, V. Buscaglia and P. Nanni, Hydrothermal synthesis of $SrTiO_3$ mesocrystals: Single crystal to mesocrystal transformation induced by topochemical reactions, *Cryst. Growth Des.*, 2012, **12**, 4450–4456.
28 N. Suzuki, M. Zakaria, N. Torad, K. Wu, Y. Nemoto and M. Imura, Synthesis of highly strained mesostructured $SrTiO_3/BaTiO_3$ composite films with robust ferroelectricity, *Chem. – Eur. J.*, 2013, **19**, 4446–4450.
29 D. Hu, H. Ma, Y. Tanaka, L. Zhao and Q. Feng, Ferroelectric mesocrystalline $BaTiO_3/SrTiO_3$ nanocomposites with enhanced dielectric and piezoelectric responses, *Chem. Mater.*, 2015, **27**, 4983–4994.
30 D. Hu, X. Kong, K. Mori, Y. Tanaka, K. Shinagawa and Q. Feng, Ferroelectric mesocrystals of bismuth sodium titanate: Formation mechanism, nanostructure, and application to piezoelectric materials, *Inorg. Chem.*, 2013, **52**, 10542–10551.
31 D. Hu, X. Niu, H. Ma, W. Zhang, G. Sewvandi, D. Yang, X. Wang, H. Wang, X. Kong and Q. Feng, Topochemical relations and piezoelectric responses of crystal-axis-oriented $BaTiO_3/CaTiO_3$ nanocomposites, *RSC Adv.*, 2017, **7**, 30807–30814.
32 D. Hu, W. Zhang, F. Yao, F. Kang, H. Cheng, Y. Wang, X. Kong, P. Wen and Q. Feng, Structural and morphological evolution of an octahedral $KNbO_3$ mesocrystal *via* self-assembly topotactic conversion process, *CrystEngComm*, 2018, **20**, 728–737.
33 F. Lotgering, Topotactical reactions with ferrimagnetic oxides having hexagonal crystal structures—I, *J. Inorg. Nucl. Chem.*, 1959, **9**, 113–123.

© 2022 The Author(s). Published by the Royal Society of Chemistry

Open Access Article. Published on 03 May 2022. Downloaded on 4/8/2025 2:31:31 AM.
This article is licensed under a Creative Commons Attribution-NonCommercial 3.0 Unported Licence.

34 S. Wada, K. Yako, T. Muraishi, K. Yokoh, S. Nam, H. Kakemoto and T. Tsurumi, Enhanced piezoelectric property of barium titanate single crystals by domain wall engineering using patterning electrode, *Ferroelectr.*, 2006, **340**, 17–24.

35 G. Krese and D. Joubert, From ultrasoft pseudopotentials to the projector agumented-wave method, *Phys. Rev. B.*, 1999, **59**, 1758.

36 P. E. Blöchl, Projector augmented-wave method, *Phys. Rev. B.*, 1994, **50**, 17953.

37 J. P. Perdew, K. Burke and M. Ernzerhof, Generalized gradient approximation made simple, *Phy. Rev. Lett.*, 1996, **77**, 3865.

38 G. Kresse and J. Furthmüller, Efficiency of ab-initio total energy calculations for metals and semiconductors using a plane-wave basis set, *Comput. Mater. Sci.*, 1996, **6**, 15–50.

39 V. I. Anisimov, J. Zaanen and O. K. Andersen, Band theory and Mott insulators: Hubbard U instead of stoner I, *Phys. Rev. B.*, 1991, **44**, 943.

40 F. Maldonado, R. Rivera, L. Villamagua and J. Maldonado, DFT modelling of ethanol on $BaTiO_3$(001) surface, *Appl. Surf. Sci.*, 2018, **456**, 276–289.

41 H. Chang and P. Huang, Thermo-Raman studies on anatase and rutile, *J. Raman Spectrosc.*, 1998, **29**, 97–102.

42 Y. Shiratori, C. Pithan, J. Dornseiffer and R. Waser, Raman scattering studies on nanocrystalline $BaTiO_3$ part I-isolated particles and aggregates, *J. Raman Spectrosc.*, 2007, **38**, 1288–1299.

43 H. Lee, S. Moon, C. Choi and D. Kim, Synthesis and size control of tetragonal barium titanate nanopowders by facile solvothermal method, *J. Am. Ceram. Soc.*, 2012, **95**, 2429–2434.

44 U. Joshi, S. Yoon, S. Baik and J. Lee, Surfactant-free hydrothermal synthesis of highly tetragonal barium titanate nanowires: A structural investigation, *J. Phys. Chem. B.*, 2006, **110**, 12249–12256.

45 F. Maxim, P. Ferreira, P. Vilarinho and L. Reaney, Hydrothermal synthesis and crystal growth studies of $BaTiO_3$ using Ti nanotube precursors, *Cryst. Growth Des.*, 2008, **8**, 3309–3315.

46 D. Hu, X. Luo, X. Kong, Y. Wang, Y. Tanaka and Q. Feng, Topochemical conversion of protonated titanate single crystals into platelike $Ba_{0.5}Sr_{0.5}TiO_3$ mesocrystals with controllable microstructures, *CrystEngComm*, 2015, **17**, 1758–1764.

47 D. Hu, K. Mori, X. Kong, K. Shinagawa, S. Wada and Q. Feng, Fabrication of [100]-oriented bismuth sodium titanate ceramics with small grain size and high density for piezoelectric materials, *J. Eur. Ceram. Soc.*, 2014, **34**, 1169–1180.

48 T. Motohashi and T. Kimura, Development of texture in $Bi_{0.5}Na_{0.5}TiO_3$ prepared by reactive-templated grain growth process, *J. Eur. Ceram. Soc.*, 2007, **27**, 3633–3636.

49 D. Maurya, Y. Zhou, Y. Yan and S. Priya, Synthesis mechanism of grain-oriented lead-free piezoelectric $Na_{0.5}Bi_{0.5}TiO_3$–$BaTiO_3$ ceramics with giant piezoelectric response, *J. Mater. Chem. C*, 2013, **1**, 2102–2111.

© 2022 The Author(s). Published by the Royal Society of Chemistry